



Investigating Periodic Table Interpolation for the Rational Design of Nanoalloy Catalysts for Green Hydrogen Production from Ammonia Decomposition

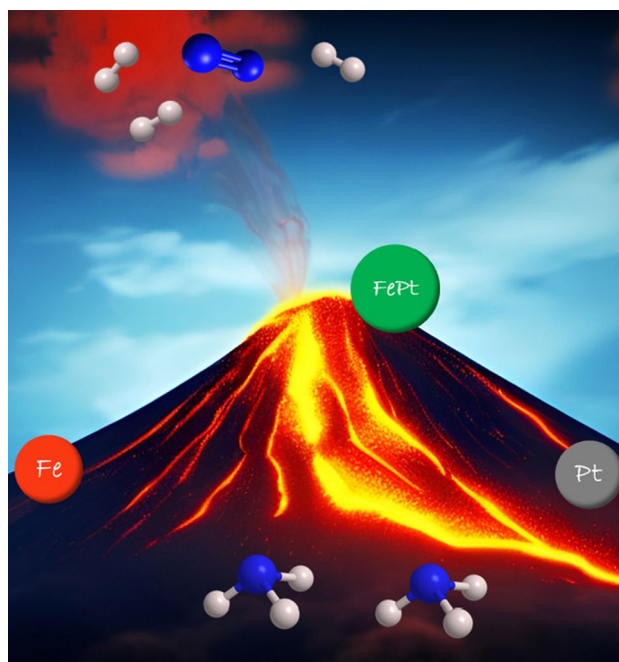
Luke A. Parker^{1,2} · Nia Richards¹ · Liam Bailey¹ · James H. Carter¹ · Ewa Nowicka¹ · Samuel Patisson¹ · Nicholas F. Dummer¹ · Qian He^{1,3} · Li Lu⁴ · Christopher J. Kiely⁴ · Stanislaw E. Golunski¹ · Alberto Roldan¹ · Graham J. Hutchings¹

Received: 18 June 2023 / Accepted: 14 August 2023
© The Author(s) 2023

Abstract

Developing highly active catalysts for the decomposition of ammonia to produce hydrogen is an important goal in the context of renewable energy. Allied with this is a need for identification strategies to efficiently design novel catalysts integral to ensuring rapid progress in this research field. We investigated the efficacy of N-binding energy and periodic table interpolation to predict active bimetallic nanoparticle catalysts. Supported iron-platinum and iron-palladium were identified and experimentally shown to be more active than their monometallic analogues. Atomic resolution electron microscopy indicated that the most active catalyst (5 wt% Fe₈₀Pt₂₀/γ-Al₂O₃) was principally formed of alloyed nanoparticles. It restructured during testing, yet no activity loss was noted at 20 h time-on-line. While these findings show that periodic table interpolation may be a viable tool for identifying active combinations of metals, the activity of the catalysts in the current work were not able to outperform the Ru/Al₂O₃ benchmark. Further catalyst optimization or refinement of reaction descriptors may facilitate the development of catalysts with higher intrinsic activity than the current state-of-the-art catalysts.

Graphical Abstract



Extended author information available on the last page of the article

Keywords Green hydrogen · Ammonia decomposition · Ammonia cracking · Catalyst design · Nanoalloys

1 Introduction

Climate change is one of the greatest challenges of our time. It is directly responsible for numerous ecological disasters, such as coral bleaching and the melting of the polar ice caps. A significant contributor to climate change is the CO₂ emitted from burning fossil fuels, which has motivated research into a clean “hydrogen economy,” as H₂ combustion will produce only clean water as a by-product. A recent Intergovernmental panel on climate change (IPCC) study reported that the environmental situation is far worse than previously thought; radical changes are required immediately to stop global temperatures increasing by 2 °C, accelerating the need for clean fuels [1].

Proton exchange membrane fuel cells (PEMFCs) can be an alternative to combustion technology. The use of hydrogen in PEMFCs produces no CO_x by-products, yielding significantly cleaner energy than combustion sources [2]. However, hydrogen fuel is limited by storage and transportation issues, requiring large storage tanks at pressures in excess of 200 bar. Thus, alternative hydrogen sources have been widely investigated [3–6]. Methanol and methane are two traditional examples of hydrogen-storing molecules; however, both produce CO_x products upon utilization. This by-product poisons the membranes of PEMFCs, and, therefore, cannot be used as a fuel source in this particular application [7, 8]. Alternatively, ammonia has been recognized as a suitable hydrogen carrier and is now being investigated as a source of H₂ for fuel cells [8–11]. Ammonia can also be liquefied at moderate pressures and ambient temperature, enabling it to be stored and transported easily, making it compatible with the current liquid fuel infrastructure [12]. However, ammonia is also a poison for PEMFCs (with tolerances of 0.1 ppm) [13], although it can be effectively removed by the use of an absorber or membrane reactor [14, 15].

Ammonia decomposition is considered a critical reaction in the search for a feasible source of hydrogen for fuel cell technology. At the point of use, ammonia can be broken down into hydrogen for fuel, with the only by-product being harmless nitrogen. However, current catalysts are often based on scarce metals such as Ru or contain complex supports unsuitable for scale-up, such as carbon nanotubes [16]. The NH₃ decomposition reaction proceeds through sequential dehydrogenation steps followed by the combinative desorption of H₂ and N₂ [17]. The rate-determining step (RDS) depends on the nitrogen binding energy, where a strong binding facilitates the N–H bond scission and a weak one facilitates

the combinative desorption of nitrogen [18]. As a result, a volcano plot of activity as a function of binding energy can be produced [18, 19]. Due to its high intrinsic activity, Ru has been widely studied, with many studies investigating the optimal particle size and active sites [20–22]. Even as a single catalyst, Ru has been shown to be the most active [23–25].

However, Ru is scarce, making it undesirable as a mass-market catalyst [26]. Periodic table interpolation theory posits that the N-binding energy of an alloy is a linear combination of that of the parent metals [19, 27]. Therefore, an optimized intermediate binding energy could be formed by alloying abundant metals with high and low N-binding energy. For the ammonia synthesis reaction, which can also be described using N-binding energy, the bio-inspired CoMo catalyst was predicted through periodic table interpolation and demonstrated to be more active than Ru [19]. CoMo is also active in the decomposition reaction [28]. It has been noted that under reaction conditions, alloys can undergo surface segregation. As such, the N-binding energy on the pristine CoMo per se can become an ineffective descriptor to predict the catalyst’s activity [27]. Metal multilayer surfaces where Ni, Fe, or Co are added to Pt(111) have also been predicted and demonstrated to be active at < 300 °C while the sub-surface configurations of the same metals (e.g. Pt–Co–Pt or Pt–Fe–Pt) were not, indicating the importance of nanostructure [27, 29].

In this work, we use periodic table interpolation based on the Sabatier principle as a design tool for preparing active catalysts, as detailed by Nørskov and co-workers [30]. To support this principle, we prepared a series of monometallic catalysts to underpin the investigation of two candidate nanoalloy catalysts (Fe–Pt and Fe–Pd). Novel-supported alloy preparation methods have garnered much attention in recent years [31–33]. Chemical vapor impregnation (CVI) is a solventless alternative to the colloidal methods more commonly employed and has been successfully applied in preparing supported nanoparticle catalysts [34–36]. CVI was employed to prepare the catalysts, which were characterized, and electron microscopy was used to investigate the nanoparticle structure of the promising Fe–Pt formulation before and after use.

2 Methods

2.1 Materials

Gamma-alumina; γ -Al₂O₃ (powder, ultra-dry; 90 m² g⁻¹), platinum(II) chloride; PtCl₂ (98%), platinum(II)

acetylacetonate; Pt(acac)₂ (97%), palladium(II) chloride; PdCl₂ (≥ 99.9%), palladium(II) acetylacetonate; Pd(acac)₂ (99%), iron(III) chloride; FeCl₃ (anhydrous for synthesis), iron(III) acetylacetonate Fe(acac)₃ (≥ 99.9%), ruthenium(III) chloride; RuCl₃ (Ru content 45–55%), ruthenium(III) acetylacetonate; Ru(acac)₃ (97%), nickel(II) chloride; NiCl₂ (98%), nickel(II) acetylacetonate; Ni(acac)₂ (95%), cobalt(II) chloride; CoCl₂ (anhydrous, ≥ 98.0%) cobalt(II) acetylacetonate; Co(acac)₂ (97%) were used as received and purchased from Merck (Sigma Aldrich). Argon, 5000 ppm NH₃/Ar and 5% H₂/Ar supplied by BOC.

2.2 Catalyst Preparation

2.2.1 Wet Impregnation

Monometallic (Ru, Fe, Ni, Co, Fe, Pt and Pd) catalysts were prepared by wet impregnation. The appropriate mass of metal chloride precursor was measured to give a 5 wt% loading. These were dissolved in de-ionised water and added to 0.95 g of dried γ-Al₂O₃ support. The mixture was stirred at 80 °C until the excess solvent was removed and the catalyst resembled a thick paste. The Co, Fe, Ni, Pd, and Ru catalysts were dried in a vacuum oven at 60 °C for 2 h. Due to safety issues with the use of chloroplatinates, the Pt catalyst was dried in a specific oven at 110 °C for 16 h. The catalysts were then reduced under a flow of 5% H₂/Ar at 550 °C with a temperature ramp rate of 10 °C min⁻¹ for 3 h.

2.2.2 Chemical Vapour Impregnation (CVI)

Monometallic (Ru, Fe and Pt) and bimetallic catalysts (FePt and FePd) with various molar ratios were prepared by chemical vapour impregnation (CVI) to prepare catalysts with a total metal loading of 5 wt%. Appropriate metal precursors (Pt(acac)₂, Pd(acac)₂, Ru(acac)₃, and/or Fe(acac)₃) were mixed with γ-Al₂O₃ in a Schlenk flask and heated to 140 °C for 1 h under vacuum. The as-prepared catalyst was reduced at 550 °C for 3 h in a flow of 5% H₂/Ar. As all catalysts in this study are 5 wt% loading and supported on γ-Al₂O₃, they will henceforth be referred to only by their molar metal ratio (*i.e.*, Pt or Fe₈₀Pt₂₀).

2.3 Ammonia Decomposition Reaction

Ammonia decomposition was carried out on pelleted and sieved catalyst samples (300–425 μm) in a quartz, fixed-bed flow reactor (*i.d.*, 7 mm; catalyst mass, 100 mg) under a flow of dilute NH₃ (5000 ppm NH₃/Ar, 100 ml/min) at 500 °C. The resultant GHSV through the catalyst bed was 60,000 h⁻¹, which was representative of the high space velocity expected to be used in catalytic NH₃-dissociation reactors. Before the reaction, the catalyst was pre-treated

under a flow of Ar (100 ml/min) at 500 °C for 1 h to remove any surface contaminants. On-line analysis of the effluent gas stream was carried out using a Gasmet DX4000 Fourier-Transform Infra-red spectrometer (FT-IR) and the H₂ formation rate was calculated after steady-state was achieved. Each reaction was carried out three times and an average used in the reaction data presented, where the error bars represent the standard deviation of each of the triplicate tests.

Equation 1 was used to calculate the ammonia conversion (C_{NH_3}) based on the difference between the moles of ammonia fed into the reactor, m_{NH_3i} , and that detected at the outlet, m_{NH_3o} :

$$C_{NH_3}(\%) = \left(\frac{m_{NH_3i} - m_{NH_3o}}{m_{NH_3i}} \right) \times 100 \quad (1)$$

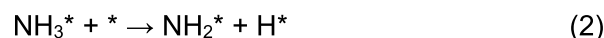
From this the H₂ formation rate was calculated according to Eq. 2:

$$\text{Formation rate of } H_2 = \left(\left(m_{NH_3i} \times \frac{C_{NH_3}}{100} \right) \times 1.5 \right) \times \text{Catalyst}_{mass\ factor} \quad (2)$$

where the formation rate of H₂ (mmol_{H₂} g⁻¹ s⁻¹) is given by the moles of ammonia fed, m_{NH_3i} (mmol s⁻¹) into the reactor as a function of NH₃ conversion, adjusted to the moles of H₂ evolved in the reaction (1.5) over 1 g of catalyst ($\text{Catalyst}_{mass\ factor} = 10$ for 100 mg of catalyst as used in this study).

2.4 Characterisation

Samples for examination by (S)TEM were prepared by dry dispersing the catalyst powder onto a holey carbon film supported by a 300 mesh copper TEM grid. Bright field (BF) TEM images were taken using a JEOL 2100FX microscope operating at 200 kV. Bright field (BF) and high angle annular



Scheme 1 Elementary steps of the ammonia decomposition reaction; * indicates surface adsorption

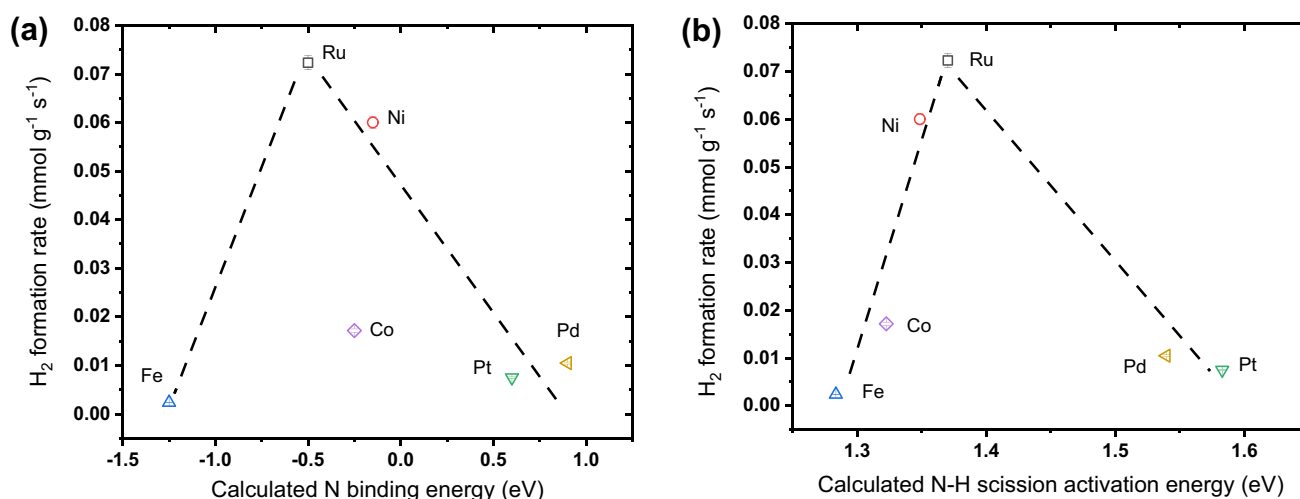


Fig. 1 Relationship between initial H₂ formation rate and N-binding energy **a** or N–H scission activation energy **b** over 5 wt% M/Al₂O₃ (M=Fe, Co, Ni, Ru, Pd or Pt), Ru at 100% conversion; Error bars represent average activity of three reactions. Reaction conditions:

100 mg_{cat}, 100 ml/min (GHSV 60000 h⁻¹), 5000 ppm NH₃/Ar, 1 atm, 500 °C, 2 h. N-binding and N–H scission activation energies are reported in ref. 30 and ref. 24 respectively

dark field (HAADF) STEM images of Fe-Pt catalysts were taken using an aberration-corrected JEM ARM-200CF microscope operating at 200 kV. This instrument was also equipped with a JEOL Centurio silicon drift detector for X-ray energy dispersive spectroscopy (XEDS). Particle size distribution analysis was performed from analysis of the HAADF electron micrographs using ImageJ.

CO-DRIFTS studies were carried out on a Bruker Tensor 27 spectrometer using a Harrick *in-situ* cell equipped with 2 mm CaF₂ windows. The cell was connected to a water chiller, Harrick cell heater and thermocouple to regulate the temperature. A 2% CO/N₂ mixture was flowed over the catalyst at room temperature at a rate of 20 ml min⁻¹ until saturated (approx. 20 min) whereupon the gas flow was switched to N₂ to purge any gas phase and physisorbed CO species. After the removal of gas-phase CO, a spectrum was recorded.

Samples were placed in metal sample holders and patterns were measured using a Panalytical X'Pert diffractometer with a Cu X-ray source operating at 40 kV and 40 mA. Patterns were attained by 40 min scans over a 2θ angular range of 5–80°. Phase identification was performed by matching experimental patterns against entries from the international centre for diffraction data (ICDD) database.

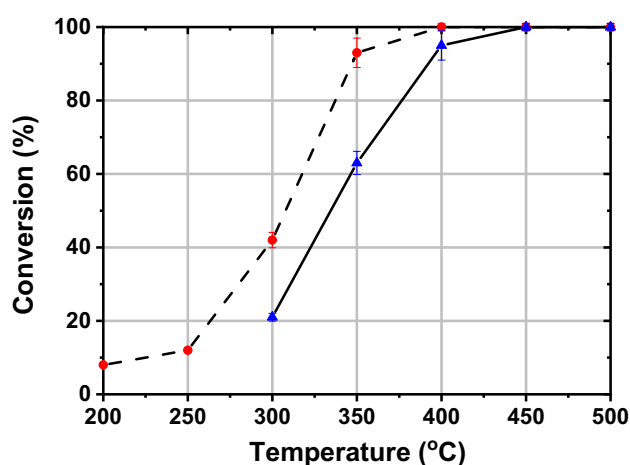


Fig. 2 Activity profile of 5 wt% Ru/Al₂O₃ catalysts prepared by CVI (red circles) and wet impregnation (blue triangles) as a function of reaction temperature. Error bars represent average activity of three reactions. Reaction conditions: 100 mg_{cat}, 100 ml/min (GHSV 60000 h⁻¹) 5000 ppm NH₃/Ar, 1 atm, 2 h

3 Results and Discussion

3.1 Relationship Between N–Binding Energy and Catalyst Activity

The interaction of atomic nitrogen with the catalysts (N-binding energy) is a suitable descriptor of catalytic activity for NH₃ synthesis and decomposition reactions [25]. Materials with N-binding energy that is not too weak or too strong are good catalyst candidates. The rationale for this

statement can be rationalized from the reaction mechanism of select elementary reactions presented in Scheme 1.

Ammonia initially adsorbs onto the catalyst's surface through the N atom (step 1). Three consecutive N–H bond scissions occur, leading to H adsorbed on the catalyst's surface (steps 2 to 4). The reaction proceeds through the associative desorption of adsorbed H and N atoms (steps 5a and b). The rate-determining step (RDS) in this mechanism is widely accepted to be either the first dehydrogenation (step 2) or the N₂ desorption (step 5b) [24], which is dependent on the N-binding energy. When the N-binding energy indicates a weak interaction, the first N–H bond is difficult to cleave, and step 2 in Scheme 1 is the RDS. As the N-binding energy increases, the electron back-donation into the N–H antibonding orbital increases, facilitating N–H bond cleavage (steps 2–4). However, strong N-binding hinders the N₂ associative desorption (5b), which becomes the RDS [37]. Such a dependence of the RDS on a physical property results in a volcano plot of activity, as introduced by Sabatier in the early 1900s, explaining the reasons behind optimum catalyst performance and design [30].

We have explored the relationship between N-binding energy and NH₃ decomposition by preparing six monometallic transition metal catalysts (Fe, Co, Ni, Ru, Pd, and Pt) supported on γ -Al₂O₃ by wet impregnation. The H₂ formation rate from NH₃ decomposition, expressed as the mmol of H₂ formed over a gram of catalyst per second, was plotted as a function of the N-binding energy values extracted from density function theory (DFT) calculations by Nørskov and co-workers [30] resulting in the volcano plot presented in Fig. 1a. The H₂ formation rates achieved in this work (Fig. 1a and b) over the monometallic catalysts are comparable to those reported in the comprehensive review by Lucentini et al. [38]. The correlation between catalytic activity and N-binding energy also follows the expected trend; Ru is the most active catalyst achieving 100% conversion at 500 °C (0.072 mmol_{H₂} g⁻¹ s⁻¹) (Fig. 1). For example, a 5% Ru/Al₂O₃ catalyst promoted with potassium (100% NH₃ inlet flow, 30,000 h⁻¹ GHSV, 400 °C) achieved an H₂ formation rate of 0.07 mmol g⁻¹ s⁻¹ [39]. In contrast, an H₂ formation rate of 0.88 mmol g⁻¹ s⁻¹ was achieved over a K-promoted 4.85% Ru supported on magnesia-carbon nanotube catalyst (100% NH₃ inlet flow, 60,000 h⁻¹ GHSV, 400 °C) [40]. The other metals with stronger/weaker N-binding energies are on either side of the highest catalyst activity. Co is an outlier; the N-binding energy implies that the NH₃ decomposition rate should be higher (Fig. 1a). We consider that this discrepancy may be due to the dispersion of the metal or possible differences between the structure of the prepared catalyst and the structure used to calculate the value of N-binding energy. It was also noted that a similar correlation was found when the catalytic activity was plotted against N–H scission

activation energy as calculated by Masel and co-workers [24] (Fig. 1b).

Despite the previous monometallic results, this study focuses on influencing the decomposition rate through rational bimetallic catalyst design [24, 30]. In both correlations, i.e. N-binding and N–H scission energies, Fe was on the opposite side of the volcano to Pd and Pt and, hence, according to periodic table interpolation, nanoalloys formed from Pt–Fe and Pd–Fe could be good candidates for NH₃ decomposition. We extend Hansgen's et al. investigation on Fe–Pt–Pt(111) surface active at low temperatures [29] to conventional nanoparticulate catalyst design. The H₂ formation rate over Fe-based catalysts indicates that it is typically low, in the order of 0.002–0.09 mmol_{H₂} g⁻¹ s⁻¹ [38]. Pt-based catalysts alloyed with Ni or Sn were reported to achieve H₂ formation rates in a range of 0.009–0.103 mmol_{H₂} g⁻¹ s⁻¹. However, a rate of 0.103 mmol_{H₂} g⁻¹ s⁻¹ was achieved at 500 °C over a PtSn/MCM-41 catalyst with an NH₃ flow rate of 250 ml min⁻¹ [41]. Higher rates were reported; however, higher temperatures were required to reach these (T₅₀ of ca. 600 °C, the temperature at which 50% conversion occurs).

3.2 Enhancing Catalyst Activity Using Chemical Vapour Impregnation as a Preparative Technique

CVI has emerged as a promising method to prepare active catalysts containing metals such as Fe and Cu [42, 43] and has also been demonstrated to be effective in preparing alloy catalysts such as PdZn [44]. The small (< 5 nm) nanoparticles typically prepared by CVI and their narrow particle size distribution suggest that it may be a viable route to preparing highly active ammonia decomposition catalysts. To validate this proposition, the activity of two Ru/Al₂O₃ catalysts, one prepared by wet impregnation and the other by CVI, were tested between 200 and 500 °C (Fig. 2). Both catalysts show ammonia decomposition activity at temperatures as low as 300 °C with the catalyst prepared by CVI showing activity at temperatures as low as 200 °C (< 10% conversion). These reaction temperatures also agree with modelled micro-kinetic simulations [45]. The CVI catalyst was more active and had a T₂₀ (the temperature at which 20% conversion occurs) of ca. 260 °C (H₂ formation rate of 0.0144 mmol g⁻¹ s⁻¹), which is roughly 40 °C lower than the T₂₀ value for the wet impregnation catalyst.

The active site for Ru catalysts has previously been identified as a B₅-type site [46]. These B₅ sites are important for ammonia synthesis and decomposition, and have also been shown to be the active site for Fischer–Tropsch synthesis and π -bond cleavage in diatomic molecules [47, 48]. Therefore, preparing Ru nanoparticles with a high concentration of B₅ sites is significant within catalysis. It

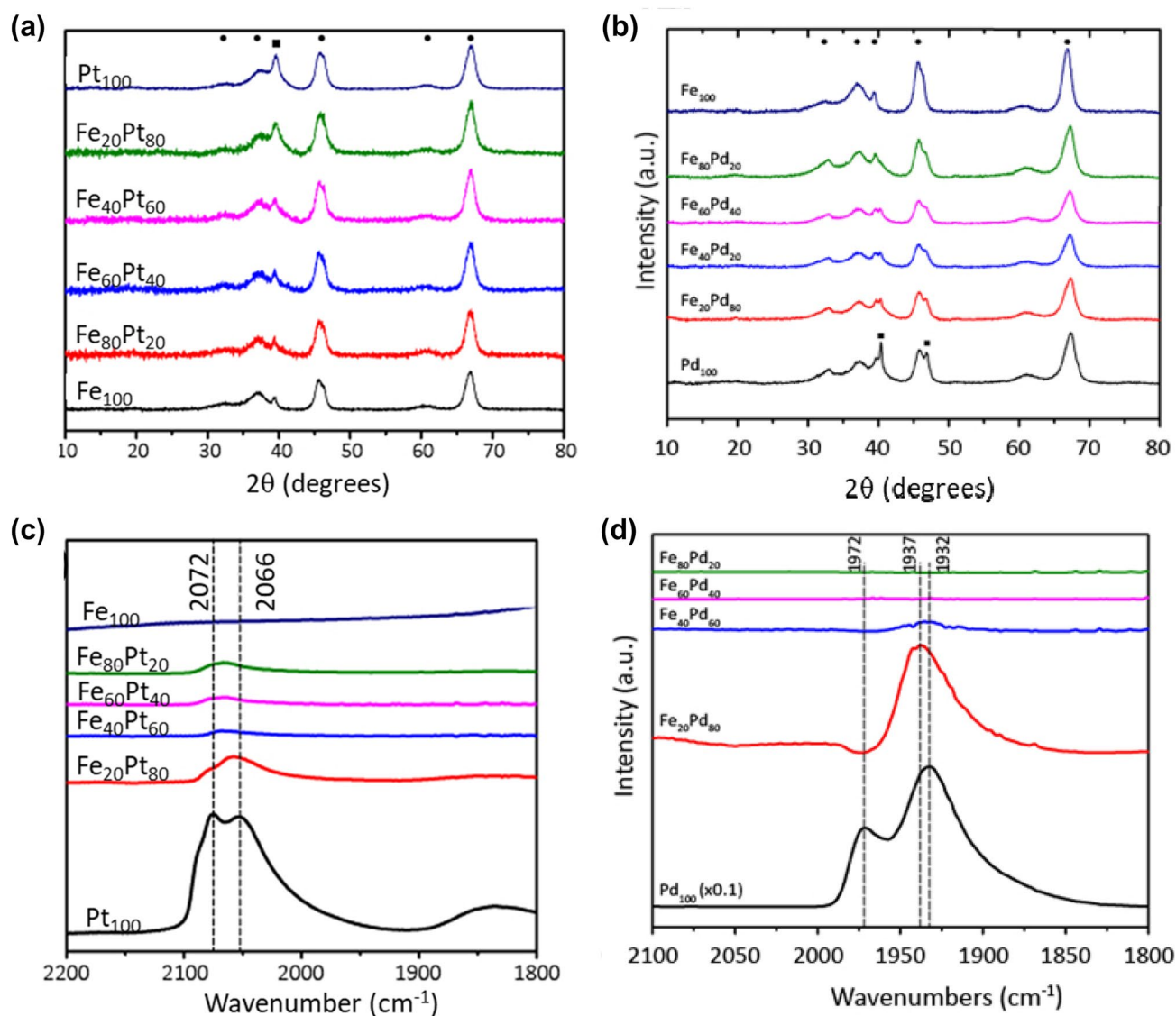


Fig. 3 Powder XRD patterns of four compositions of FePt **a** and FePd **b**, and the two-parent mono-metals supported on γ -Al₂O₃; reflections labeled (filled circle) originate from γ -Al₂O₃. The region labeled (filled square) corresponds to where Pt(111) or Pd(111) and

Al₂O₃(222) reflections are found. CO-DRIFTS spectra of the four compositions of FePt **c** and FePd **d** catalysts and their parent metals supported on γ -Al₂O₃

has also been shown that the optimum particle size for B₅ site formation is 3–5 nm [21]. This difference in reactivity between CVI and wet impregnation routes may be related to the number of B₅ sites and the crystal structure of the nano-catalysts, as shown previously [45, 49]. Representative bright field TEM images of both Ru/Al₂O₃ catalysts are shown in Figure S1. Both methods produce Ru particles that are well-dispersed. The mean Ru particle size was 2.47 nm (average from 100 nanoparticles) when prepared by wet impregnation and 2.62 nm (average from 101 nanoparticles) when prepared by CVI. Although the difference in average particle size is small, it is consistent with the catalytic activity comparison (Fig. 2) of the 5 wt% Ru/Al₂O₃ catalysts

prepared by CVI and IWI. Hence, CVI is chosen to be the main catalyst preparation method used throughout the paper as it can lead to well-dispersed supported nanoparticles and it is solvent-free.

3.3 Evaluation of Nanoalloys with Different Rate-Determining Steps

As illustrated in Fig. 1, monometallic Fe, Pd, and Pt catalysts are relatively inactive (<0.01 mmol_{H₂} g⁻¹ h⁻¹). The rate-determining step is the N₂ associative desorption over Fe, whereas it is the N–H bond scission over Pt and Pd. We prepared a systematic set of Fe–Pt and Fe–Pd catalysts

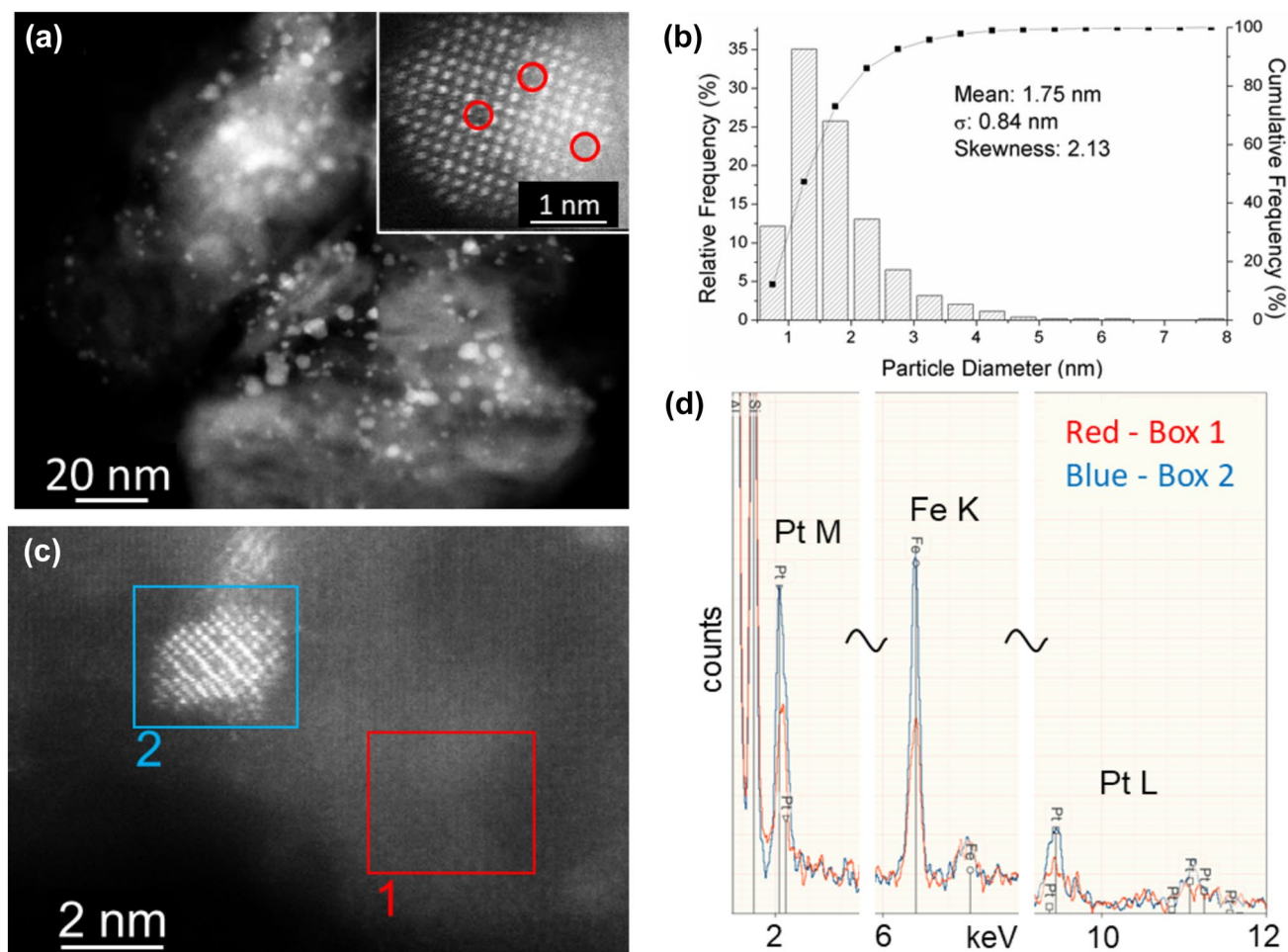


Fig. 4 Representative HAADF-STEM image of the unused $\text{Fe}_{80}\text{Pt}_{20}/\text{Al}_2\text{O}_3$ catalyst **a** and its corresponding particle size distribution (diameter) **b**. The higher magnification image shown inset in **a** displays some atomic columns highlighted in red with relatively lower contrast and are considered Fe-rich columns in the FePt particle. **c**

An additional HAADF-STEM image and the corresponding X-ray Energy Dispersive Spectra from areas 1 and 2 highlighted in **d** demonstrate that the particle labeled 2 contains both Fe and Pt

with various nominal compositions via CVI to investigate the catalysts' design efficacy using N-binding energy and periodic table interpolation. Preparation of both Fe-Pt and Fe-Pd alloys in several molar percentages (namely, $\text{Fe}_{20}\text{M}_{80}$, $\text{Fe}_{40}\text{M}_{60}$, $\text{Fe}_{60}\text{M}_{40}$, and $\text{Fe}_{80}\text{M}_{20}$, where $\text{M}=\text{Pd}$ or Pt) was achieved. Initially, the catalyst synthesis via CVI was performed sequentially with an impregnation of $\text{Fe}(\text{acac})_3$ followed by a reduction step and a subsequent impregnation with $\text{Pt}(\text{acac})_2$ before a final reduction step. Analysis of powder XRD patterns (Fig. S3) and TEM images (Fig. S4) suggested that this led to a considerable amount of unalloyed Pt, which formed large nanoparticles, the diameter of which progressively decreased as the Pt content of the alloy decreased. The evidence for the Pt nanoparticles being alloyed is based on the sharp reflections in Figure S4 of the seq-CVI catalysts assigned to Pt(111), where the $\text{Fe}_3\text{Pt}(111)$ reflection would be found at 40.3° . Therefore, all subsequent

preparations were carried out by a co-CVI method whereby both metals were impregnated simultaneously, followed by a single reduction step under flowing 5% H_2/Ar at 550°C .

The powder XRD patterns of the supported series of co-CVI FePt catalysts with varying compositions, shown in Fig. 3a, display six broad reflections at 2θ values of 32° , 37° , 39° , 47° , 62° and 68° , which correspond to the (220), (311), (222), (400), (333) and (440) planes respectively of the $\gamma\text{-Al}_2\text{O}_3$ support [50]. As the Pt content of the catalyst increases, an overlapping reflection at $2\theta=39^\circ$ appears due to Pt(111), suggesting that some large, unalloyed Pt particles may still be present [51]. See Figure S3 for XRD of the support only. DRIFTS spectra with carbon monoxide (CO-DRIFTS) as probe molecule were recorded on the Fe, Pt, and FePt samples to assess the structure of the metal surface (Fig. 3c). In the Pt-only catalyst, two peaks with centers at 2052 and 2076 cm^{-1} are noted and attributed to CO adsorbed

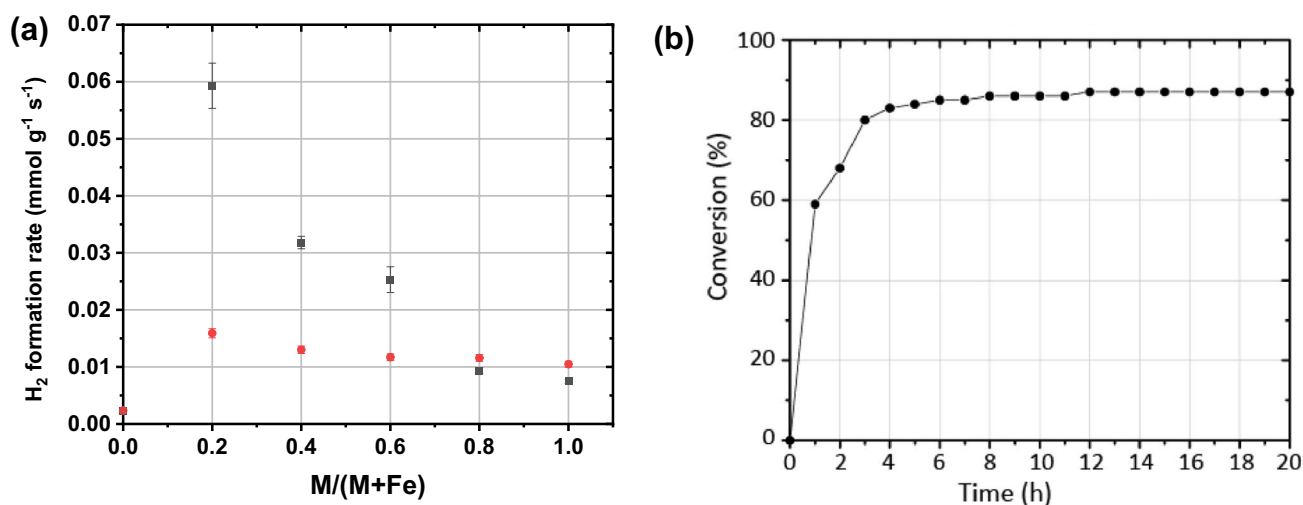


Fig. 5 H₂ formation rate as a function of nominal Pt/(Pt+Fe) (black square) and Pd/(Pd+Fe) (red circle) ratio at 2 h time-on-line **a** Error bars represent average activity of three reactions. Time-on-line (20 h)

of NH₃ conversion over Fe₈₀Pt₂₀/Al₂O₃ catalyst at 500 °C **b** Reaction conditions: 100 mg_{cat}, 100 ml/min (GHSV 60000 h⁻¹), 5000 ppm NH₃/Ar, 1 atm

on Pt atoms associated with edge and kink sites, respectively [52]. These are consistent with the presence of small Pt particles as analyzed from the XRD data. The intensity of these two peaks decreased dramatically upon the introduction of Fe, suggesting that fewer of these sites are available for the binding of CO. At Fe-rich compositions (*i.e.*, >Fe₄₀), these peaks become lower in intensity and indistinguishable from the background profile. These observations indicate that most Pt was now alloyed with Fe, with only a lower concentration of isolated Pt sites remaining to bind CO.

The fresh Fe₈₀Pt₂₀ sample was analyzed using STEM. Representative images are displayed in Fig. 4a and c, and S5, with the corresponding particle size distribution in Fig. 4b. The XEDS results in Fig. 4d confirm that the prepared particles are indeed nano-alloys and that they are small and well-dispersed with a mean particle diameter of 1.75 nm (average from 536 particles). The larger (> 5 nm) particles present have a low population, and the overall population is dominated by particles with a diameter of < 3 nm. The HAADF-STEM image in Fig. 4a (inset) suggests some limited atomic ordering of the Fe and Pt in the nano-alloys may be occurring with this particle exposing the {100} and {110} facets of tetragonal FePt. EDS data in Fig. 4c and d, where the background region (red box) shows a Fe:Pt composition ratio of 82:18 and the particle (blue box) shows a Fe:Pt ratio of 83:17, confirmed that the molar ratio of Fe:Pt in the nanoparticle was close to that of the nominal ratio. This confirms the particles contain both Fe and Pt, and also suggests that Fe and Pt are likely to be present across the support surface, possibly atomically dispersed (a proposition supported by CO-DRIFTS measurements). These

measurements indicate the potential to improve the nano-alloy formation's efficiency further.

The catalytic activity over the series of Fe-Pt catalysts is shown in Fig. 5a. As previously indicated, the parent metals were both relatively inactive at 500 °C where respective H₂ formation rates over Fe and Pt were 0.002 and 0.007 mmol g⁻¹ s⁻¹. However, a synergistic effect can be seen for the nano-alloy catalysts, which all outperformed the parent metals. The most active catalyst was Fe₈₀Pt₂₀, which achieved ca. 82% conversion (H₂ formation rate 0.06 mmol g⁻¹ s⁻¹) under the same reaction conditions. As discussed earlier, the alloy composition influences the efficiency of alloy formation; as the Fe content of the catalysts increases, the extent of alloying increases, resulting in a higher number of active nano-alloy sites and fewer, less active, unalloyed metal particles. However, it is recognized that metal dispersion and the efficiency of alloying present additional complexities, particularly when preparing supported nanoparticle catalysts. Furthermore, while the alloyed catalysts did not achieve the same activity level as the Ru catalyst, it demonstrates that two inactive metals can be used to form active NH₃ decomposition catalysts, and further optimization of the catalyst may reduce the activity gap between FePt and Ru. Indeed, Hansgen et al. demonstrated through both theoretical and NH₃-TPD experiments that Fe-Pt-Pt(111) was a highly active bimetallic composition, capable of decomposing NH₃ at < 77 °C [29], highlighting the importance of nanostructure.

The stability of the most active (Fe₈₀Pt₂₀) catalyst was also assessed by running the ammonia decomposition reaction at 500 °C continuously for 20 h (Fig. 5b). During that time, no significant deactivation was observed, and the

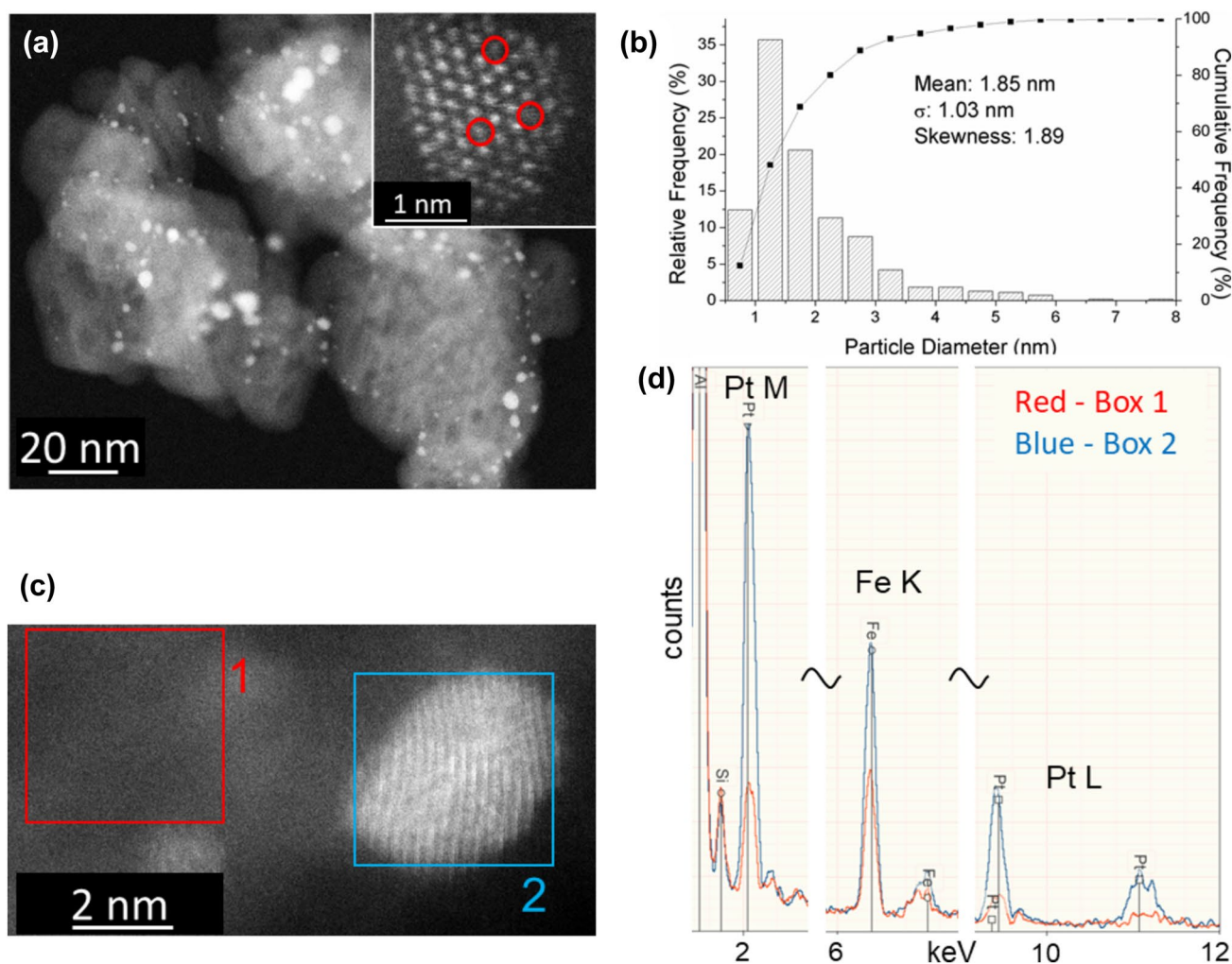


Fig. 6 Representative HAADF-STEM images of the used $\text{Fe}_{80}\text{Pt}_{20}/\text{Al}_2\text{O}_3$ catalyst **a** and its corresponding particle size distribution (diameter) **b** A higher magnification HAADF image is shown as an inset in **a**, and some atomic columns with relatively lower contrast

(implying they are Fe-rich) are highlighted in red. **c** An additional HAADF-STEM image and the corresponding X-ray Energy Dispersive Spectra from areas 1 and 2 are highlighted in **c**

activity profile suggests that the catalyst improved over the initial 4 h. We note that the time-on-line test at such a low concentration of NH_3 does not truly reflect the stability of the overall catalyst activity. The catalyst may have taken time to reach steady-state operation during this initial period, which prompted us to analyze the recovered post-use catalyst by STEM imaging (Figs. 6a and S6) and XEDS analysis (Fig. 6c, d). Figure 6b shows that after 20 h testing, the mean particle diameter was 1.85 nm, an insignificant increase from the fresh catalyst (1.75 nm). This test indicated that Fe-Pt nano-alloys prepared by CVI are not only small and well-dispersed when prepared but also resistant to sintering under reaction conditions and any other deactivation mechanism. However, we note that the nanoparticles underwent structural changes during the reaction, transforming from well-faceted, structured particles to random alloys. This

restructuring could be responsible for the modest improvement in NH_3 conversion from 1 to 4 h time-on-line.

Pd has a similar calculated N-binding energy to Pt, meaning that the rate-determining step over Pd should also be N-H bond scission. It was expected that FePd nanoalloy catalysts would show similar results to these of FePt catalysts, namely a synergistic effect resulting in a higher conversion of ammonia. Four FePd catalysts were prepared similarly to the FePt catalysts and were characterized by powder XRD as shown in Fig. 3b. Five characteristic reflections due to $\gamma\text{-Al}_2\text{O}_3$ were observed. However, there were also two reflections at 2θ values of 39.9° and 46.6° attributed to Pd^0 (100) and (200), respectively [53]. These signals indicate that the conditions of the preparation method were not ideal for the FePd catalysts and resulted in larger crystallites of Pd. The intensity of these peaks decreases

as the Fe-content increases, suggesting that the extent of alloying increases or that the size of the Pd nanoparticles decreases.

CO-DRIFTS of the FePd series was performed to elucidate further the effect of the metal composition on the properties of the metal. The monometallic Pd sample exhibits two bands centered at 1979 and 1940 cm^{-1} (Fig. 3d). These are attributed to the bridging modes of CO on metallic Pd [54, 55]. Interestingly, no linearly bound CO was observed, expected at $>2000 \text{ cm}^{-1}$, suggesting that surface Pd atoms were present in the catalyst or, more likely, that alloying with Fe caused a significant electronic modification of the metal nanoparticle that inhibited CO adsorption. After the introduction of Fe, the band at 1979 cm^{-1} observed in monometallic Pd disappeared, and the overall intensity of the adsorbed CO decreased by an order of magnitude. The lower stability of the bridged species at 1970 cm^{-1} has been previously reported [54]. Furthermore, as the Fe-content of the FePd alloy catalysts increased, the band at 1940 cm^{-1} decreased and was not visible in the $\text{Fe}_{60}\text{Pd}_{40}$ and $\text{Fe}_{80}\text{Pd}_{20}$ samples. It is thought that, as the Fe content of the catalyst increased, the extent of the alloying increased, and these bands decreased due to a lack of neighbouring Pd sites on the surface, similar to that observed with the FePt series (Fig. 3c).

From the FePd catalytic activity (Fig. 3a), it is evident that all the FePd samples were less active than their FePt analogues. However, there are some similarities between the two sets of testing data, which indicates that there may be a critical compositional-related synergistic effect of alloyed metals with differing rate-determining steps. Firstly, all the nano-alloy catalysts show synergy compared to the monometallic catalysts. Secondly, the most active nanoalloy catalyst was $\text{Fe}_{80}\text{Pd}_{20}$, achieving a conversion of 23% (H_2 formation rate $0.016 \text{ mmol g}^{-1} \text{ s}^{-1}$). The origin of this effect may be due to the formation of catalysts with a more optimized N-binding energy, but this might not have been achieved as efficiently as with the counterpart FePt catalyst series despite the comparable N-binding energies of Pd and Pt. This suggests that other factors affect the catalytic activity, such as Fe-Pd mixing or nanoparticle size, which were not optimized in relation to $\text{Fe}_{80}\text{Pt}_{20}$. It is also significant that in both nano-alloy catalysts, the activity was not as high as Ru, which illustrates the complexity of catalyst design comprised of multiple metals.

4 Conclusions

Using the CVI preparation method, we have demonstrated a simple, solvent-free route for preparing mono- and bi-metallic nanoparticles and show that it leads to a narrow distribution of nanoparticle diameter. By considering the N-binding energy

as an activity descriptor for NH_3 decomposition, we identified FePt and FePd as promising bimetallic catalysts, which exhibited higher activity than the parent metals. Although the FePt catalyst was not as active as a monometallic Ru catalyst, we have shown that two inactive metals can be combined to form active NH_3 decomposition catalysts. Furthermore, there is scope to improve the efficiency of alloy formation, which could close the activity gap to Ru catalysts. While necessary for the potential hydrogen economy through their application in ammonia decomposition, these results have a broad appeal to the general catalysis field. The methods utilized apply to many reactions governed by scaling relationships to design novel nano-alloy catalysts with the potential to outperform current benchmarks.

Supplementary Information The online version contains supplementary material available at <https://doi.org/10.1007/s10562-023-04446-4>.

Acknowledgements We would like to thank the ERC for financial support through the funding project *After the GoldRush*: project number ERC-AtG-291319. C.J.K. gratefully acknowledges funding from the National Science Foundation Major Research Instrumentation program (GR# MRI/DMR-1040229). We thank the Max Planck Society and the Cardiff University for financial support to create the FUNCAT Centre. AR acknowledge the financial support from the EPSRC-funded UK Interdisciplinary centre for Circular Chemical Economy (NIC3E) (EP/V011863/1).

Funding ERC, ERC-AtG-291319

Declarations

Conflict of interest The authors declare no competing financial interest.

Open Access This article is licensed under a Creative Commons Attribution 4.0 International License, which permits use, sharing, adaptation, distribution and reproduction in any medium or format, as long as you give appropriate credit to the original author(s) and the source, provide a link to the Creative Commons licence, and indicate if changes were made. The images or other third party material in this article are included in the article's Creative Commons licence, unless indicated otherwise in a credit line to the material. If material is not included in the article's Creative Commons licence and your intended use is not permitted by statutory regulation or exceeds the permitted use, you will need to obtain permission directly from the copyright holder. To view a copy of this licence, visit <http://creativecommons.org/licenses/by/4.0/>.

References

1. IPCC (2022) Summary for Policymakers. Global warming of 1.5 °C: IPCC Special report on impacts of global warming of 1.5 °C above pre-industrial levels in context of strengthening response to climate change sustainable development and efforts to eradicate poverty. Cambridge University Press, Cambridge, pp 1–24

- Mehta V, Cooper JS (2003) Review and analysis of PEM fuel cell design and manufacturing. *J Power Sources* 114:32–53. [https://doi.org/10.1016/S0378-7753\(02\)00542-6](https://doi.org/10.1016/S0378-7753(02)00542-6)
- Eberle U, Felderhoff M, Schüth F (2009) Chemical and physical solutions for hydrogen storage. *Angew Chem Int Ed* 48:6608–6630. <https://doi.org/10.1002/anie.200806293>
- Joó F (2008) Breakthroughs in hydrogen storage—formic acid as a sustainable storage material for hydrogen. *Chemoschem* 1:805–808. <https://doi.org/10.1002/cssc.200800133>
- Rosi NL, Eckert J, Eddaoudi M, Vodak DT, Kim J, O’Keeffe M, Yaghi OM (2003) Hydrogen storage in microporous metal-organic frameworks. *Science* 300:1127–1129. <https://doi.org/10.1126/science.1083440>
- Sakintuna B, Lamari-Darkrim F, Hirscher M (2007) Metal hydride materials for solid hydrogen storage: a review. *Int J Hydrogen Energy* 32:1121–1140. <https://doi.org/10.1016/j.ijhydene.2006.11.022>
- Choudhary TV, Goodman DW (2002) CO-free fuel processing for fuel cell applications. *Catal Today* 77:65–78. [https://doi.org/10.1016/S0920-5861\(02\)00233-X](https://doi.org/10.1016/S0920-5861(02)00233-X)
- Yin S-F, Zhang Q-H, Xu B-Q, Zhu W-X, Ng C-F, Au C-T (2004) Investigation on the catalysis of CO_x-free hydrogen generation from ammonia. *J Catal* 224:384–396. <https://doi.org/10.1016/j.jcat.2004.03.008>
- Choudhary TV, Sivadinarayana C, Goodman DW (2001) Catalytic ammonia decomposition: CO_x-free hydrogen production for fuel cell applications. *Catal Lett* 72:197–201. <https://doi.org/10.1023/A:1009023825549>
- Durbin DJ, Malardier-Jugroot C (2013) Review of hydrogen storage techniques for on board vehicle applications. *Int J Hydrogen Energy* 38:14595–14617. <https://doi.org/10.1016/j.ijhydene.2013.07.058>
- Smith C, Torrente-Murciano L (2021) Guidance for targeted development of ammonia synthesis catalysts from a holistic process approach. *Chem Catalysis* 1:1163–1172. <https://doi.org/10.1016/j.checat.2021.09.015>
- Valera-Medina A, Banares-Alcantara R (2020) Techno-economic challenges of green ammonia as an energy vector -, 1st edn. Academic Press
- Miyaoka H, Miyaoka H, Ichikawa T, Ichikawa T, Kojima Y (2018) Highly purified hydrogen production from ammonia for PEM fuel cell. *Int J Hydrogen Energy* 43:14486–14492. <https://doi.org/10.1016/j.ijhydene.2018.06.065>
- Chellappa AS, Fischer CM, Thomson WJ (2002) Ammonia decomposition kinetics over Ni-Pt/Al₂O₃ for PEM fuel cell applications. *Appl Catal A* 227:231–240. [https://doi.org/10.1016/S0926-860X\(01\)00941-3](https://doi.org/10.1016/S0926-860X(01)00941-3)
- García-García FR, Ma YH, Rodríguez-Ramos I, Guerrero-Ruiz A (2008) High purity hydrogen production by low temperature catalytic ammonia decomposition in a multifunctional membrane reactor. *Catal Commun* 9:482–486. <https://doi.org/10.1016/j.catcom.2007.07.036>
- Wang SJ, Yin SF, Li L, Xu BQ, Ng CF, Au CT (2004) Investigation on modification of Ru/CNTs catalyst for the generation of CO_x-free hydrogen from ammonia. *Appl Catal B* 52:287–299. <https://doi.org/10.1016/j.apcatb.2004.05.002>
- Ertl G, Huber M (1980) Mechanism and kinetics of ammonia decomposition on iron. *J Catal* 61:537–539. [https://doi.org/10.1016/0021-9517\(80\)90403-0](https://doi.org/10.1016/0021-9517(80)90403-0)
- Boisen A, Dahl S, Nørskov JK, Christensen CH (2005) Why the optimal ammonia synthesis catalyst is not the optimal ammonia decomposition catalyst. *J Catal* 230:309–312. <https://doi.org/10.1016/j.jcat.2004.12.013>
- Jacobsen CJH, Dahl S, Clausen BS, Bahn S, Logadottir A, Nørskov JK (2001) Catalyst design by interpolation in the periodic table: bimetallic ammonia synthesis catalysts. *J Am Chem Soc* 123:8404–8405. <https://doi.org/10.1021/ja010963d>
- Hill AK, Torrente-Murciano L (2014) In-situ H₂ production via low temperature decomposition of ammonia: Insights into the role of cesium as a promoter. *Int J Hydrogen Energy* 39:7646–7654. <https://doi.org/10.1016/j.ijhydene.2014.03.043>
- García-García FR, Guerrero-Ruiz A, Rodríguez-Ramos I (2009) Role of B5-Type Sites in Ru Catalysts used for the NH₃ Decomposition Reaction. *Top Catal* 52:758–764. <https://doi.org/10.1007/s11244-009-9203-7>
- Arevalo RL, Aspera SM, Escaño MCS, Nakanishi H, Kasai H (2017) First principles study of methane decomposition on B5 step-edge type site of Ru surface. *J Phys: Condens Matter* 29:184001. <https://doi.org/10.1088/1361-648X/aa66c7>
- Li L, Zhu ZH, Yan ZF, Lu GQ, Rintoul L (2007) Catalytic ammonia decomposition over Ru/carbon catalysts: the importance of the structure of carbon support. *Appl Catal A* 320:166–172. <https://doi.org/10.1016/j.apcata.2007.01.029>
- Ganley JC, Thomas FS, Seebauer EG, Masel RI (2004) A priori catalytic activity correlations: the difficult case of hydrogen production from ammonia. *Catal Lett* 96:117–122. <https://doi.org/10.1023/B:CATL.0000030108.50691.d4>
- Bell TE, Torrente-Murciano L (2016) H₂ production via ammonia decomposition using non-noble metal catalysts: a review. *Top Catal* 59:1438–1457. <https://doi.org/10.1007/s11244-016-0653-4>
- Ravi M, W. Makepeace J (2022) Facilitating green ammonia manufacture under milder conditions: what do heterogeneous catalyst formulations have to offer? *Chem Sci* 13:890–908. <https://doi.org/10.1039/D1SC04734E>
- Hansgen DA, Vlachos DG, Chen JG (2010) Using first principles to predict bimetallic catalysts for the ammonia decomposition reaction. *Nature Chem* 2:484–489. <https://doi.org/10.1038/nchem.626>
- Duan X, Qian G, Zhou X, Chen D, Yuan W (2012) MCM-41 supported CoMo bimetallic catalysts for enhanced hydrogen production by ammonia decomposition. *Chem Eng J* 207–208:103–108. <https://doi.org/10.1016/j.cej.2012.05.100>
- Hansgen DA, Thomanek LM, Chen JG, Vlachos DG (2011) Experimental and theoretical studies of ammonia decomposition activity on Fe-Pt, Co-Pt, and Cu-Pt bimetallic surfaces. *J Chem Phys* 134:184701. <https://doi.org/10.1063/1.3589260>
- Medford AJ, Vojvodic A, Hummelshøj JS, Voss J, Abild-Pedersen F, Studt F, Bligaard T, Nilsson A, Nørskov JK (2015) From the Sabatier principle to a predictive theory of transition-metal heterogeneous catalysis. *J Catal* 328:36–42. <https://doi.org/10.1016/j.jcat.2014.12.033>
- Mizukoshi Y, Fujimoto T, Nagata Y, Oshima R, Maeda Y (2000) Characterization and catalytic activity of core-shell structured gold/palladium bimetallic nanoparticles synthesized by the sonochemical method. *J Phys Chem B* 104:6028–6032. <https://doi.org/10.1021/jp994255e>
- Kim D, Resasco J, Yu Y, Asiri AM, Yang P (2014) Synergistic geometric and electronic effects for electrochemical reduction of carbon dioxide using gold-copper bimetallic nanoparticles. *Nat Commun* 5:4948. <https://doi.org/10.1038/ncomms5948>
- Wong A, Liu Q, Griffin S, Nicholls A, Regalbutto JR (2017) Synthesis of ultrasmall, homogeneously alloyed, bimetallic nanoparticles on silica supports. *Science* 358:1427–1430. <https://doi.org/10.1126/science.aao6538>
- Sun S, Murray CB, Weller D, Folks L, Moser A (2000) Monodisperse FePt nanoparticles and ferromagnetic FePt Nanocrystal Superlattices. *Science* 287:1989–1992. <https://doi.org/10.1126/science.287.5460.1989>

35. Wang C, Hou Y, Kim J, Sun S (2007) A general strategy for synthesizing FePt nanowires and nanorods. *Angew Chem Int Ed* 46:6333–6335. <https://doi.org/10.1002/anie.200702001>
36. Chen M, Pica T, Jiang Y-B, Li P, Yano K, Liu JP, Datye AK, Fan H (2007) Synthesis and self-assembly of fcc phase FePt Nanorods. *J Am Chem Soc* 129:6348–6349. <https://doi.org/10.1021/ja069057x>
37. Lu X, Roldan A (2021) Are carbon-based materials good supports for the catalytic reforming of ammonia? *The Journal of Physical Chemistry C*. <https://doi.org/10.1021/acs.jpcc.1c03996>
38. Lucentini I, Garcia X, Vendrell X, Llorca J (2021) Review of the decomposition of ammonia to generate hydrogen. *Ind Eng Chem Res* 60:18560–18611. <https://doi.org/10.1021/acs.iecr.1c00843>
39. Su Q, Gu LL, Zhong AH, Yao Y, Ji WJ, Ding WP, Au CT (2018) Layered double hydroxide derived Mg2Al-LDO supported and K-modified Ru catalyst for hydrogen production via ammonia decomposition. *Catal Lett* 148:894–903. <https://doi.org/10.1007/s10562-017-2195-1>
40. Yin SF, Xu BQ, Wang SJ, Ng CF, Au CT (2004) Magnesia-carbon nanotubes (MgO–CNTs) nanocomposite: novel support of ru catalyst for the generation of cox-free hydrogen from ammonia. *Catal Lett* 96:113–116. <https://doi.org/10.1023/B:CATL.0000030107.64702.74>
41. Varisli D, Rona T (2012) COx Free hydrogen production from ammonia decomposition over platinum based siliceous materials. *Int J Chem Reactor Eng*. <https://doi.org/10.1515/1542-6580.3058>
42. Forde MM, Armstrong RD, McVicker R, Wells PP, Dimitratos N, He Q, Lu L, Jenkins RL, Hammond C, Lopez-Sanchez JA, Kiely CJ, Hutchings GJ (2014) Light alkane oxidation using catalysts prepared by chemical vapour impregnation: tuning alcohol selectivity through catalyst pre-treatment. *Chem Sci* 5:3603–3616. <https://doi.org/10.1039/C4SC00545G>
43. Forde MM, Armstrong RD, Hammond C, He Q, Jenkins RL, Kondrat SA, Dimitratos N, Lopez-Sanchez JA, Taylor SH, Willock D, Kiely CJ, Hutchings GJ (2013) Partial oxidation of ethane to oxygenates using Fe- and Cu-containing ZSM-5. *J Am Chem Soc* 135:11087–11099. <https://doi.org/10.1021/ja403060n>
44. Bahruji H, Bowker M, Jones W, Hayward J, Esquius JR, Morgan DJ, Hutchings GJ (2017) PdZn catalysts for CO₂ hydrogenation to methanol using chemical vapour impregnation (CVI). *Faraday Discuss* 197:309–324. <https://doi.org/10.1039/C6FD00189K>
45. Lu X, Zhang J, Chen W-K, Roldan A (2021) Kinetic and mechanistic analysis of NH₃ decomposition on Ru(0001), Ru(111) and Ir(111) surfaces. *Nanoscale Adv* 3:1624–1632. <https://doi.org/10.1039/D1NA00015B>
46. Zheng W, Zhang J, Xu H, Li W (2007) NH₃ decomposition Kinetics on supported Ru clusters: morphology and particle size effect. *Catal Lett* 119:311–318. <https://doi.org/10.1007/s10562-007-9237-z>
47. Van Santen RA (2009) Complementary structure sensitive and insensitive catalytic relationships. *Acc Chem Res* 42:57–66. <https://doi.org/10.1021/ar800022m>
48. van Hardeveld R, van Montfoort A (1966) The influence of crystallite size on the adsorption of molecular nitrogen on nickel, palladium and platinum: an infrared and electron-microscopic study. *Surf Sci* 4:396–430. [https://doi.org/10.1016/0039-6028\(66\)90016-1](https://doi.org/10.1016/0039-6028(66)90016-1)
49. Li X-K, Ji W-J, Zhao J, Wang S-J, Au C-T (2005) Ammonia decomposition over Ru and Ni catalysts supported on fumed SiO₂, MCM-41, and SBA-15. *J Catal* 236:181–189. <https://doi.org/10.1016/j.jcat.2005.09.030>
50. Lippens BC, De Boer JH (1964) Study of phase transformations during calcination of aluminum hydroxides by selected area electron diffraction. *Acta Crystallogr A* 17:1312–1321. <https://doi.org/10.1107/S0365110X64003267>
51. Mukerjee S, Srinivasan S, Soriaga MP, McBreen J (1995) Effect of preparation conditions of Pt alloys on their electronic, structural, and electrocatalytic activities for oxygen reduction - XRD, XAS, and electrochemical studies. *J Phys Chem* 99:4577–4589. <https://doi.org/10.1021/j100013a032>
52. Raskó J (2003) CO-induced surface structural changes of Pt on oxide-supported Pt catalysts studied by DRIFTS. *J Catal* 217:478–486. [https://doi.org/10.1016/S0021-9517\(03\)00147-7](https://doi.org/10.1016/S0021-9517(03)00147-7)
53. Xu L, Wu X-C, Zhu J-J (2008) Green preparation and catalytic application of Pd nanoparticles. *Nanotechnology* 19:305603. <https://doi.org/10.1088/0957-4484/19/30/305603>
54. Wang X, Shi H, Kwak JH, Szanyi J (2015) Mechanism of CO₂ hydrogenation on Pd/Al₂O₃ catalysts: kinetics and transient DRIFTS-MS studies. *ACS Catal* 5:6337–6349. <https://doi.org/10.1021/acscatal.5b01464>
55. Zeinalipour-Yazdi CD, Willock DJ, Thomas L, Wilson K, Lee AF (2016) CO adsorption over Pd nanoparticles: a general framework for IR simulations on nanoparticles. *Surf Sci* 646:210–220. <https://doi.org/10.1016/j.susc.2015.07.014>

Publisher's Note Springer Nature remains neutral with regard to jurisdictional claims in published maps and institutional affiliations.

Authors and Affiliations

Luke A. Parker^{1,2} · Nia Richards¹ · Liam Bailey¹ · James H. Carter¹ · Ewa Nowicka¹ · Samuel Pattison¹ · Nicholas F. Dummer¹ · Qian He^{1,3} · Li Lu⁴ · Christopher J. Kiely⁴ · Stanislaw E. Golunski¹ · Alberto Roldan¹ · Graham J. Hutchings¹

✉ Graham J. Hutchings
hutch@cardiff.ac.uk

¹ Max Planck Cardiff Centre–Fundamentals of Heterogeneous Catalysis FUNCAT, Translational Research Hub, Cardiff University, Maindy Road, Cardiff CF244HQ, UK

² Present Address: TNO Environmental Modelling, Sensing and Analysis, Princetonlaan 6, 3584CB Utrecht, The Netherlands

³ Present Address: Department of Materials Science and Engineering, National University of Singapore, 9 Engineering Drive 1, Block EA #03-09, Singapore, Singapore

⁴ Department of Materials Science and Engineering, Lehigh University, 5 E Packer Avenue, Bethlehem, PA, USA